Scripta Materialia 219 (2022) 114890

Contents lists available at ScienceDirect

Scripta Materialia

journal homepage: www.journals.elsevier.com/scripta-materialia

Increasing the yield strength while preserving strain hardenability and ductility in a beta titanium alloy exhibiting transformation induced plasticity (TRIP)

M.S.K.K.Y. Nartu [a,b], A. Sharma [a,b], S.A. Mantri [a,b], R.S. Haridas [a], Y Ren [c], R. Banerjee [a,b,*]

[a] Department of Materials Science and Engineering, University of North Texas, Denton, TX, USA
[b] Center of Agile and Adaptive Additive Manufacturing, University of North Texas, Denton, TX, USA
[c] X-ray Science Division, Advanced Photon Source, Argonne National Laboratory, IL 60439, USA

ARTICLE INFO

Keywords:
Ti-1023
Metastable beta titanium alloys
TRIP/TWIP
Martensite
Cold rolling

ABSTRACT

The commercial β-Ti alloy, Ti-10V-2Fe-3Al; primarily used with an α+β microstructure, exhibits a high yield strength but with poor strain-hardenability and limited ductility. This paper focuses on the interplay between stress-induced martensite (α") in this alloy, introduced via prior cold-rolling (5,10, 20, and 30%) and additional martensite (α") forming during subsequent tensile loading, leading to a simple way to substantially increase the yield strength while enhancing the high strain hardenability (via TRIP) and maintaining the uniform tensile ductility. The results indicate that the YS in this alloy can be substantially tuned from 400 to 1800 MPa, via cold-rolling. Among the various conditions that were analyzed, the 5% cold-rolled condition offered the best combination of YS (~900 MPa), ductility (8%) and the strain hardenability. The stress-induced α" formation during tensile loading is essential for maintaining the high strain-hardening and, consequently the uniform tensile ductility in this alloy.

The demand for high-strength β−titanium alloys is growing significantly to design high-performance, lightweight, and fuel-efficient vehicles for aerospace applications. Solid solution strengthening [1,2], precipitation strengthening via secondary α/ω phases [3–5], and cold-working [6] are possibly the three main approaches to strengthening β-titanium alloys. While the first two approaches have been extensively studied [7], there are few studies discussing strengthening via cold-working. Typically, in case of cold-worked alloys, the increase in yield strength is accompanied by a significant loss in ductility [8]. Additionally, the enhancement in yield strength obtained via cold-working of the alloys can be rather limited [9], as exhibited by those β-titanium alloys whose plasticity is dominated by dislocation slip. However, this may not be the case in those alloys which deform via TRIP (Transformation induced plasticity) and TWIP (Twinning induced plasticity) [10,11].

Ti-10V-2Fe-3Al (all in wt.%) is a high-strength metastable β-titanium alloy that essentially deforms via TRIP and TWIP in its β-solutionized and quenched state [12,13]. It exhibits significant strain hardenability and ductility but relatively low yield strengths under uniaxial tensile loading [2,14]. The relatively low stability of the β-phase results in stress-induced martensite (SIM) $\beta \rightarrow \alpha''$ transformation, which is mainly responsible for the high strain hardenability observed [15,16]. Several approaches were shown in the past to enhance the yield strength of this alloy [2,3,17]. Annealing in the α+β phase field can improve the yield strength but significantly compromises the alloy's ductility and strain hardenability [2,18]. During annealing, the α precipitates tend to reject the β-stabilizers into the β-matrix, which increases the β-phase stability. This changes the deformation mechanism from TRIP/TWIP to dislocation mediated plasticity and subsequently compromises the alloy's strain hardenability [15,16]. Danard et al. have designed a strategy to anneal the forged alloy in α+β phase-field to potentially increase the yield strength while preserving TWIP/TRIP and the associated strain hardening [19]. In this article, we present a more straightforward alternative strategy, cold-working via rolling, to enhance the mechanical properties of Ti-10V-2Fe-3Al. A detailed microstructural investigation is performed to understand the differences in the Stress-Induced Products (SIP) formed during the cold-rolling versus uniaxial tensile deformation.

A forged ingot of Ti-10V-2Fe-3Al was procured from ATI Corporation. Five bars, sectioned from the received material, were β-solution

* Corresponding author.
E-mail addresses: mohansaikirannartu@my.unt.edu (M.S.K.K.Y. Nartu), Raj.Banerjee@unt.edu (R. Banerjee).

https://doi.org/10.1016/j.scriptamat.2022.114890
Received 14 April 2022; Received in revised form 14 June 2022; Accepted 21 June 2022
Available online 25 June 2022

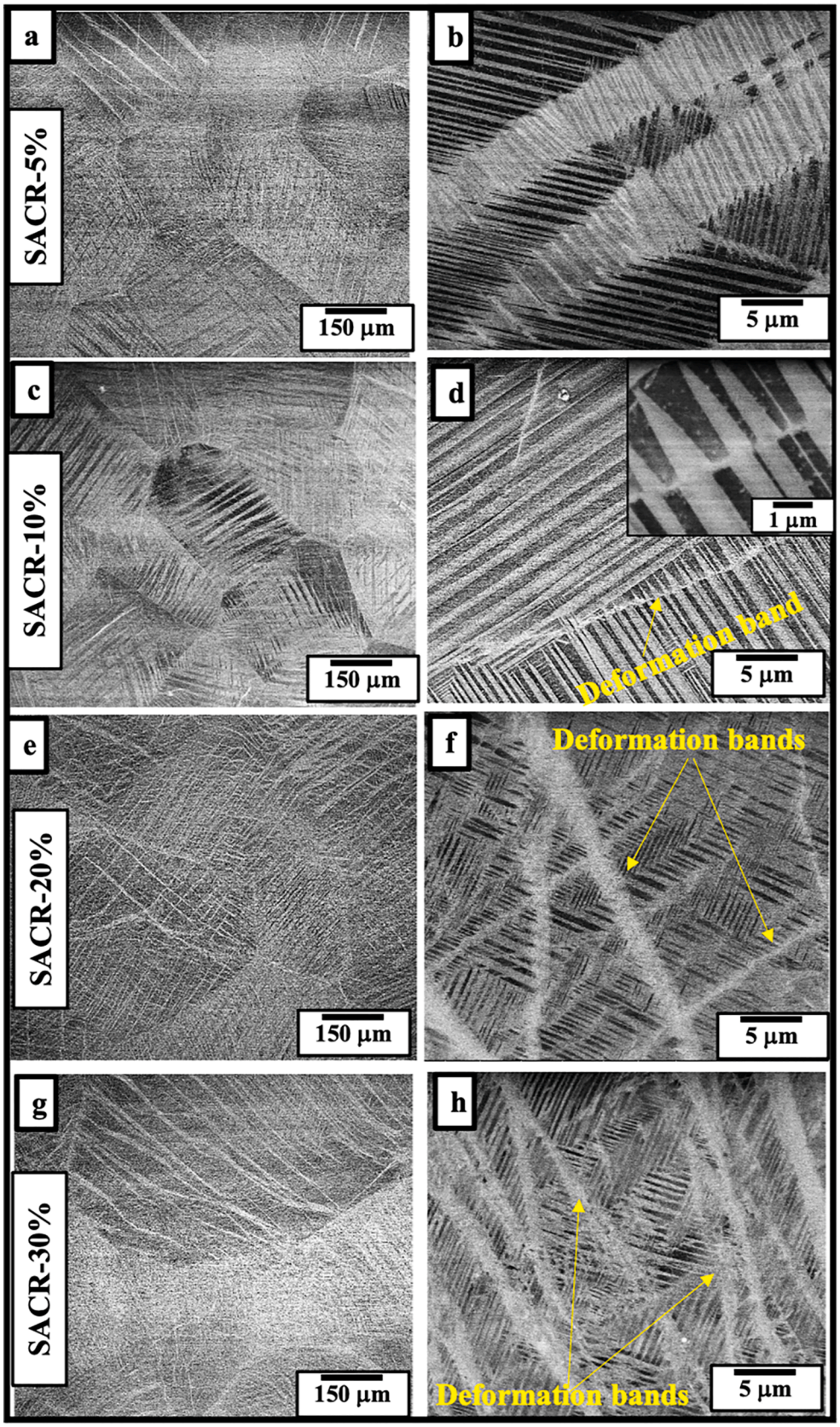

Fig. 1. SEM backscatter images for various cold rolled conditions: (a,b) SACR-5%, (c,d) SACR-10%, (e,f) SACR-20% and (g,h) SACR-30% conditions.

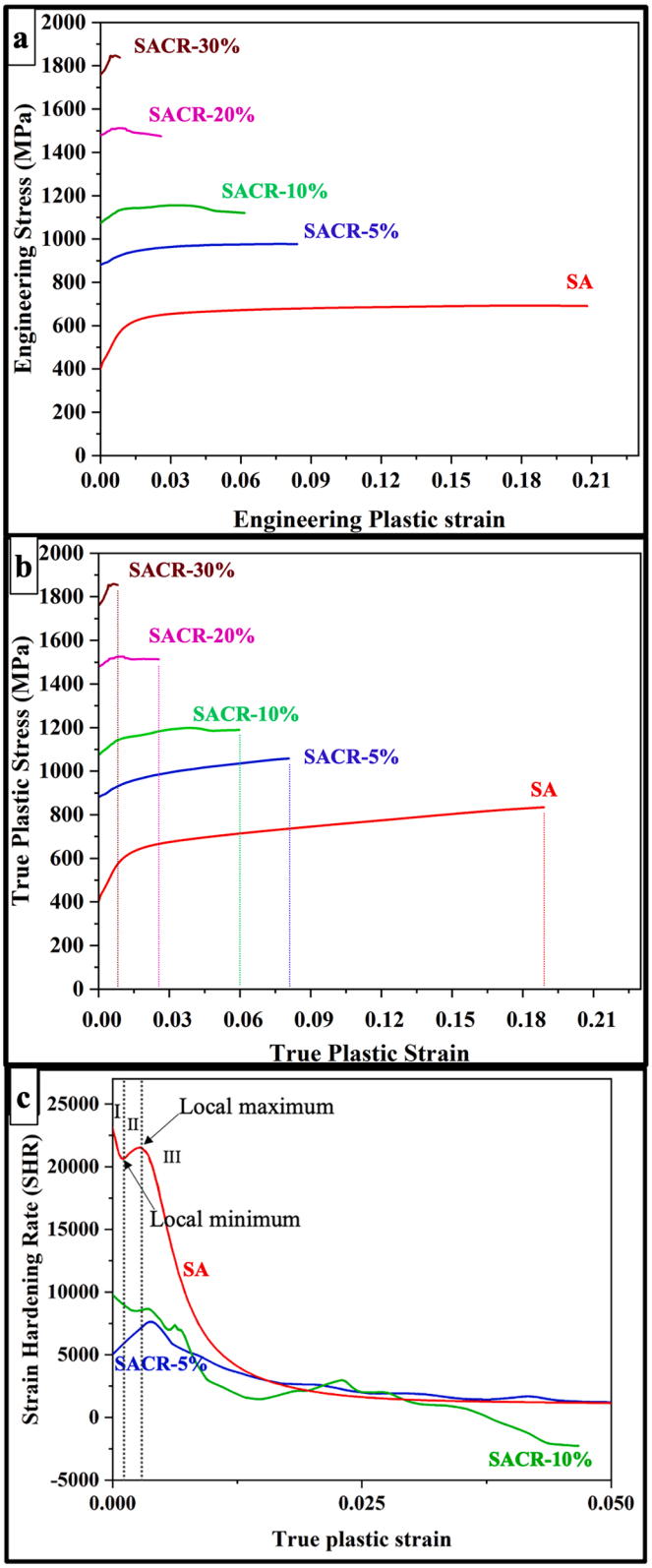

Fig. 2. The (a) Engineering stress- Engineering plastic strain, (b) True stress - True plastic strain and (c) Strain hardening rate plots for various cold-rolled conditions of Ti-1023.

annealed at 900 °C for 30 min and then quenched in water, this condition will be hereafter referred to as SA. Subsequently, four out of these five bars were cold-rolled to various percentages 5, 10, 20, 30, which will be referred to as SACR-5%, SACR-10%, SACR-20%, and SACR-30%, respectively. Mini tensile specimens of 5 mm gage length and 1 mm gage width were machined from all five conditions and tests were performed at a strain rate of 10^{-3}/s. Imaging and Electron backscatter diffraction (EBSD) analysis was performed in an FEI-Quanta Nova-Nano SEM 230. OIM™ software was used to produce the Inverse Pole Figure (IPF) maps and Phase maps from EBSD scans. TEM foils were prepared inside an FEI Nova 200 Nanolab dual-beam Focused ion beam (FIB/SEM) and were characterized using FEI Tecnai G2 F20 ST S/TEM. Further, high energy SR-XRD was performed on select conditions at the Advanced Photon Source (APS) on the 11-ID-C beamline at Argonne National Laboratory using a monochromatic 105.5 keV ($\lambda = 0.117300$ Å) x-ray beam with a beam size of 200 × 200 μm^2. The beam exposure time was approximately 0.1 s averaged over ten frames, and calibration of the SR-XRD experiments was performed using a standard CeO_2 powder.

The SEM backscatter images from the β-solutionized condition, i.e., SA, are shown in Supplementary Figure S1. The microstructure appears to be single-phase (β) devoid of any second-phase precipitates in the grain interiors or along the grain boundaries. Figs. 1(a,b), 1(c,d), 1(e,f) and 1(g,h) represent the low and high magnification SEM backscatter images from various cold-rolled conditions. The SEM images show plate or lathlike features within the β-grains for all four conditions. These lathlike features could be the α'' phase formed during the cold rolling of the alloy. While such sharp features are present in all four conditions, wavy-like deformation bands are mainly found in the significantly cold-rolled alloys, i.e., SACR-20% and SACR-30% conditions. The high magnification SEM backscatter images (Figs. 1(b,d,f,h)) clearly show the increase in the density of the deformation bands with an increase in the percentage of cold-rolling. Further, the deformation bands clearly seem to shear the martensite laths creating offsets along the length of the band, as shown in the inset in Fig. 1(d). While one would expect that with an increasing amount of cold-work, the fraction of SIM (α'') would also increase, this is not presently evident from the SEM images shown in Fig. 1. However, an assessment of the relative change in α''phase fraction was carried out using synchrotron-based X-ray diffraction analysis, which is presented later in this paper.

Uniaxial tensile tests were performed on all the conditions to investigate the effect of cold-rolling on the mechanical properties. The engineering stress-plastic strain and the true stress-plastic strain plots for all the conditions are shown in Fig. 2(a) and 2(b), respectively. A clear trend of increase in yield strength with an increase in the percentage of cold-rolling is observed. While the β-solutionized condition (SA) shows the lowest yield strength of 400 MPa, the 30% cold-rolled condition (SACR-30%) exhibits the highest yield strength of 1780 MPa. The ductility, on the other hand, seems to decrease with an increase in the extent of cold-rolling; the SA exhibits the highest ductility ~21%, followed by ~8% and ~6% exhibited by SACR-5% and SACR-10% conditions, respectively. A significant loss in ductility is observed in the samples rolled to 20% and 30%; the SACR-20% condition exhibits a ductility of ~3%, and the SACR-30% condition does not exhibit any appreciable ductility. The true stress-true strain curves have been plotted up to the point of necking and therefore the elongation values mentioned above correspond to uniform elongation. The strain hardening rate (SHR) plots for SA, SACR-5%, and SACR-10%, are shown in Fig. 2(c). The SHR plot for the SA condition clearly exhibits local minima and local maxima points. The local minimum corresponds to the onset of the SIM (α'') transformation while the local maximum represents the near saturation of the same during uniaxial tensile loading. Previous reports indicate that deformation is dominated by dislocation slip (within the β-matrix) in Region I and SIM transformation (of the β−matrix)/(TRIP) in Region II (Fig. 2(b)) [20,21]. There could still be some amount of SIM transformation of the β-phase beyond the local maximum, i.e., in Region III, but the deformation occurs mainly via dislocation slip within the retained β−matrix and the transformed α'' and also via deformation twinning within the α'' laths. The SHR plot for SACR-5% condition exhibits Regions II and III, but the SHR plot for SACR-10% condition shows only Region III (Fig. 2(b)). This possibly

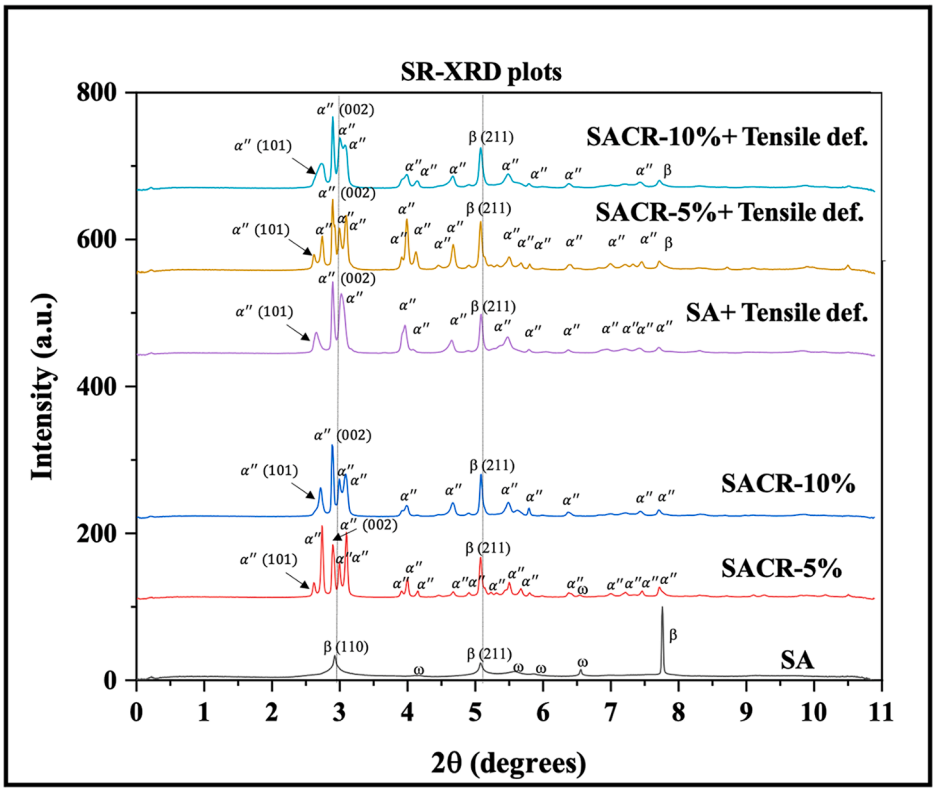

Fig. 3. SR-XRD plots (before and after tensile deformation) for SA, SACR-5%, and SACR-10% conditions.

Table 1
The peak intensity ratios, I(002)α"/I(211)β, for SA, SACR-5%, and SACR-10% conditions of Ti-1023 alloy.

Condition	Peak intensity ratio
	I(002)α"/I(211)β
SA	0
SA + Tensile Deform.	1.80
SACR-5%	1.29
SACR-5%+Tensile Deform.	1.8
SACR-10%	1.67
SACR-10%+Tensile Deform.	1.72

suggests that there could be a significant amount of α'' formed in the SACR-5% condition, while only a negligible amount of α" was formed in the SACR-10% condition during uniaxial tensile deformation.

A qualitative analysis of phase fraction and texture of α''-martensite, formed during cold-rolling and uniaxial tensile loading, was performed via SR-XRD. SR-XRD plots for SA, SACR-5%, and SACR-10% conditions are shown in Fig. 3. The presence of β and athermal-ω phases can be clearly observed in the SA condition, which agrees well with literature reports [12]. The peaks corresponding to α'' are observed in the cold-rolled as well as the tensile tested conditions, confirming the evolution of α'' during plastic deformation. The peak intensity ratios, I(002)α"/I(211)β, for SA, SACR-5%, and SACR-10% conditions are listed in Table 1. There is a clear indication of an increase in phase fraction of α'' with an increase in the extent of cold-rolling, i.e., I(002)α"/I(211)β ratio increases from 0 in SA condition to 1.29 and 1.67 in SACR-5% and SACR-10% conditions, respectively. After uniaxial tensile testing, the SACR-5% condition showed a considerable increment in the ratio (from 1.29 to 1.8), but the SACR-10% condition hardly showed any noticeable increase (from 1.67 to 1.72). This indicates that there is a substantial formation of α'' during tensile deformation of the SACR-5% condition compared to the almost negligible formation of α" in SACR-10% condition corroborating the results from SHR analysis.

The EBSD and TEM results before and after tensile deformation for the SACR-5% condition are presented in Fig. 4. The phase map from EBSD analysis, shown in Fig. 4(a), identifies the α'' laths (phase fraction ~23%) formed in the β−matrix during cold-rolling. Fig. 4(b) shows a low-magnification dark-field image of the TEM foil, highlighting the α'' laths, recorded from the spot indicated in the $[0\bar{1}\ \bar{1}]$ α''zone axis diffraction pattern shown in the inset. A DFTEM image, recorded from a region away from the α'' laths within the β matrix in the foil (indicated in Fig. 4(b)) is shown in Fig. 4(c). This dark-field image has been recorded from the superlattice spot in the diffraction pattern, shown in the inset. The diffraction pattern is obtained from the [110]β zone axis (ZA), and the superlattice spots at 1/3 and 2/3 [112]β locations in the pattern correspond to the ω phase. The DFTEM image in Fig. 4(c) shows the fine-scale (athermal) ω precipitates formed during the quenching from β−phase field prior to the cold-rolling. The SIM transformation of the β-matrix results in the shearing of the ω precipitates; therefore, the ω precipitates are only found in the untransformed β-regions. An apparent increase in the phase fraction of α'' (~50% increment) due to tensile deformation is observed in the EBSD phase map shown in Fig. 4(d). A dark-field TEM image (Fig. 4(e)) recorded from a diffraction spot corresponding to α'' (outlined in the inset) in the [111]β // [110]α''ZA, features a single coarse α'' lath along with multiple fine α'' laths within the β-matrix. The multiple fine-scale α'' laths, revealed in Fig. 4(e), are possibly forming during the tensile loading and are substantially more refined than the ones developed during the prior cold-rolling (Fig. 4(b)). The DFTEM image (Fig. 4(f)) recorded from the fundamental spot corresponding to the β−phase (outlined in the inset) reveals the untransformed β-matrix after the tensile deformation of the SACR-5% condition.

A similar analysis was performed on the SACR-10% condition, and the results are presented in Fig. 5. The phase map in Fig. 5(a) suggests a significant transformation (up to ~85%) of the β-matrix to α'' martensite due to the (10%) cold rolling which validates the SR-XRD analysis (Table 1). The high magnification DFTEM image (Fig. 5(b)) from the as-rolled condition of the SACR-10% sample reveals multiple

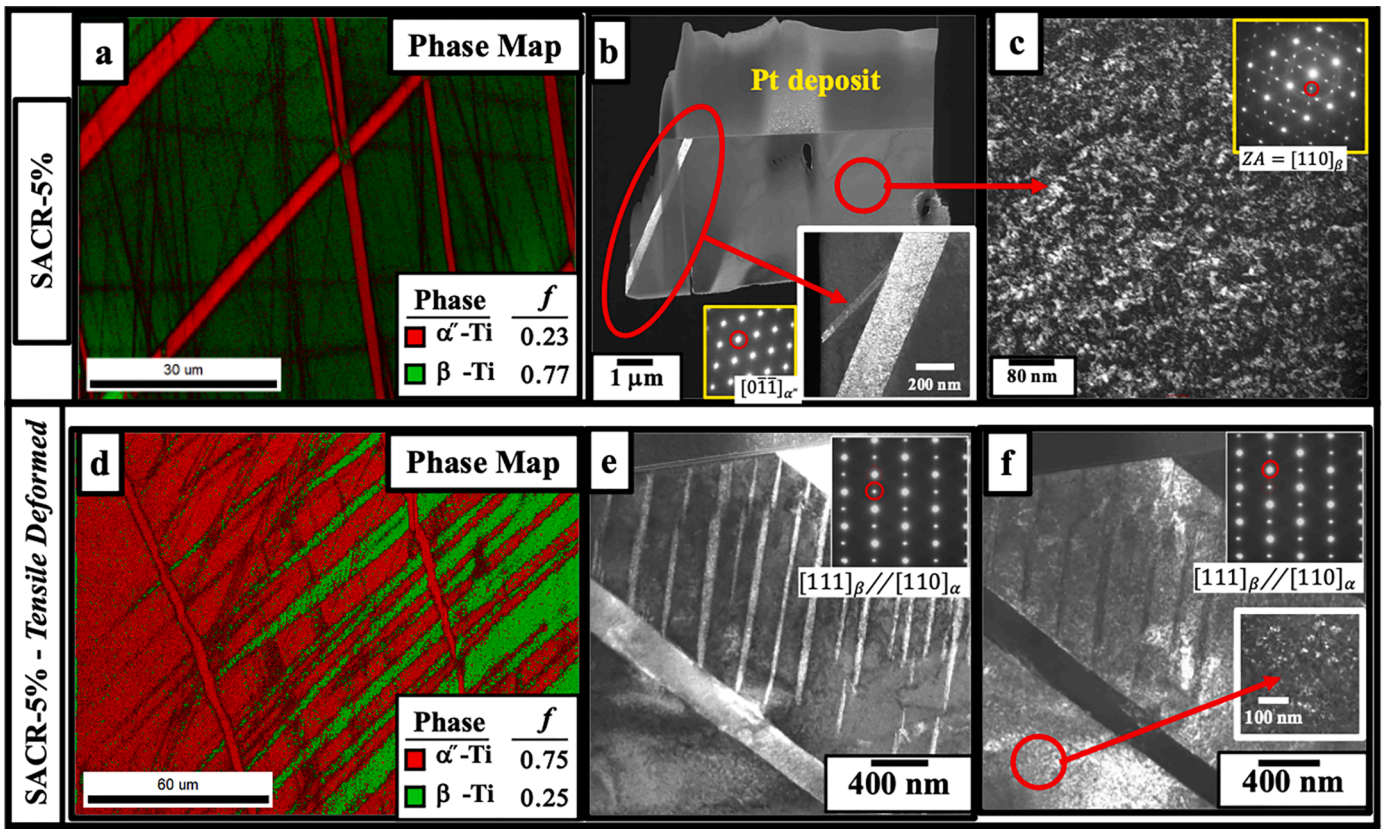

Fig. 4. (a) Phase Map identifying the α'' laths formed in the β−matrix of the SACR-5% condition during the prior cold-rolling, (b) low-magnification DFTEM image, highlighting the α'' laths formed in the same condition, recorded from the spot indicated in the $[0\bar{1}\ \bar{1}]$ α'' ***SAED*** pattern shown in the inset and (c) high magnification DFTEM image, recorded from a region away from the α'' laths within the β matrix from the same foil shown in Fig. 4(b). (d) Phase Map identifying the α'' laths formed in the β−matrix of the SACR-5% condition during the uniaxial tensile loading, (e) DFTEM image recorded from a superlattice spot corresponding to α" (outlined in the inset) in the [111]β // [110]α" ZA and (f) DFTEM image recorded from the fundamental spot corresponding to the β−phase (outlined in the inset) from the same condition (SACR-5% Tensile Deformed).

fine-scale α'' laths, identical to the SACR-5% condition after tensile deformation (Fig. 4(e)). This suggests that regardless of the mode of deformation (cold-rolling or uniaxial tensile loading) when the applied stress is greater than the triggering stress for SIM, coarser α'' laths begin to form initially, followed by more refined laths within the untransformed β-regions to accommodate the strain resulting from deformation. Therefore, the high strain hardening under tensile loading observed in the SA, and SACR-5% conditions (Fig. 2(c)) can be attributed to the formation of multiple generations of the SIM α'' laths [15,22,23] .

The high magnification DFTEM image in Fig. 5(c) highlights the β-regions that essentially remained untransformed after 10% cold-rolling. Based on the SR-XRD and SHR analyses, it appears that the near saturation of SIM formation occurred during the (10%) cold rolling itself, and hence there is no apparent additional transformation of β *to* α'' during subsequent tensile testing. Consequently, there is no TRIP effect contributing to increasing the SHR or the overall plasticity (Fig. 2 (c)) during tensile deformation (Table 1). Surprisingly, however, a significant ductility of ~6% is observed in the SACR-10% condition under tensile loading; and the underlying reason has therefore been investigated via TEM. The diffraction pattern obtained from the overlap of [111]β ZA // [110]α''ZA is shown in Fig. 5(d) with an α'' spot circled in red. The low and high magnification dark-field TEM images recorded from this α'' spot are shown in Figs. 5(e) and 5(f), respectively. The high magnification image (Fig. 5(f)) shows significant dislocation activity within the α'' laths. This indicates that, under tensile loading, the SACR-10% condition deforms predominantly via dislocation slip (within the α'' laths) with possibly negligible TRIP (in the remanent β matrix).

Additional experiments have been conducted to critically assess the differences in the strengthening mechanisms in this alloy, resulting from α'' formation (e.g., SACR-5% condition) versus the more commonly employed α precipitation. The SA alloys have been annealed at two different temperatures, i.e., 700 C and 750 C for 4 h (followed by water quenching) for α precipitation (within the β matrix). The stress-strain behaviors for SA+700 C/4 h, SA+750 C/4 h, and SACR-5% conditions have been presented in Supplementary Fig. S2. Comparing these stress-strain plots (Fig. S2(a)), it should be noted that yield stress for the two $\alpha + \beta$ annealed conditions is close to the yield stress of $\alpha''+\beta$ condition (SACR-5%). However, both the $\alpha + \beta$ conditions exhibit substantially lower ductility of ~2% as compared to ~8% in the case of $\alpha''+\beta$ condition. Furthermore, there is very limited strain-hardenability in the two $\alpha + \beta$ conditions, as shown in the work-hardening plots in Fig. S2(b). Based on the results from $\alpha + \beta$ conditions, it is expected that a significant increase in yield strength (to ~900 MPa) results in a significant decrease in the ductility (to ~2%). However, in case of the $\alpha''+\beta$ condition, a similar yield stress ~ 900 MPa (for SACR-5% condition) maintains a substantially higher ductility of ~8%. Therefore, it can be concluded that the stress-induced α''formation during tensile loading is essential for maintaining the high strain-hardening and, consequently the uniform tensile ductility in this alloy.

This difference in stress-strain behaviors can be rationalized based on the compositional partitioning between the α/β phases versus the lack of such a difference between the α''/β phases. The pronounced compositional partitioning between the α and β phases is evident in the back-scatter SEM images shown in Figs. S2(c) and (d), the brighter contrast of the β matrix indicates V and Fe enrichment within the matrix, while the darker contrast in α phase indicates Al enrichment. V and Fe stabilize the

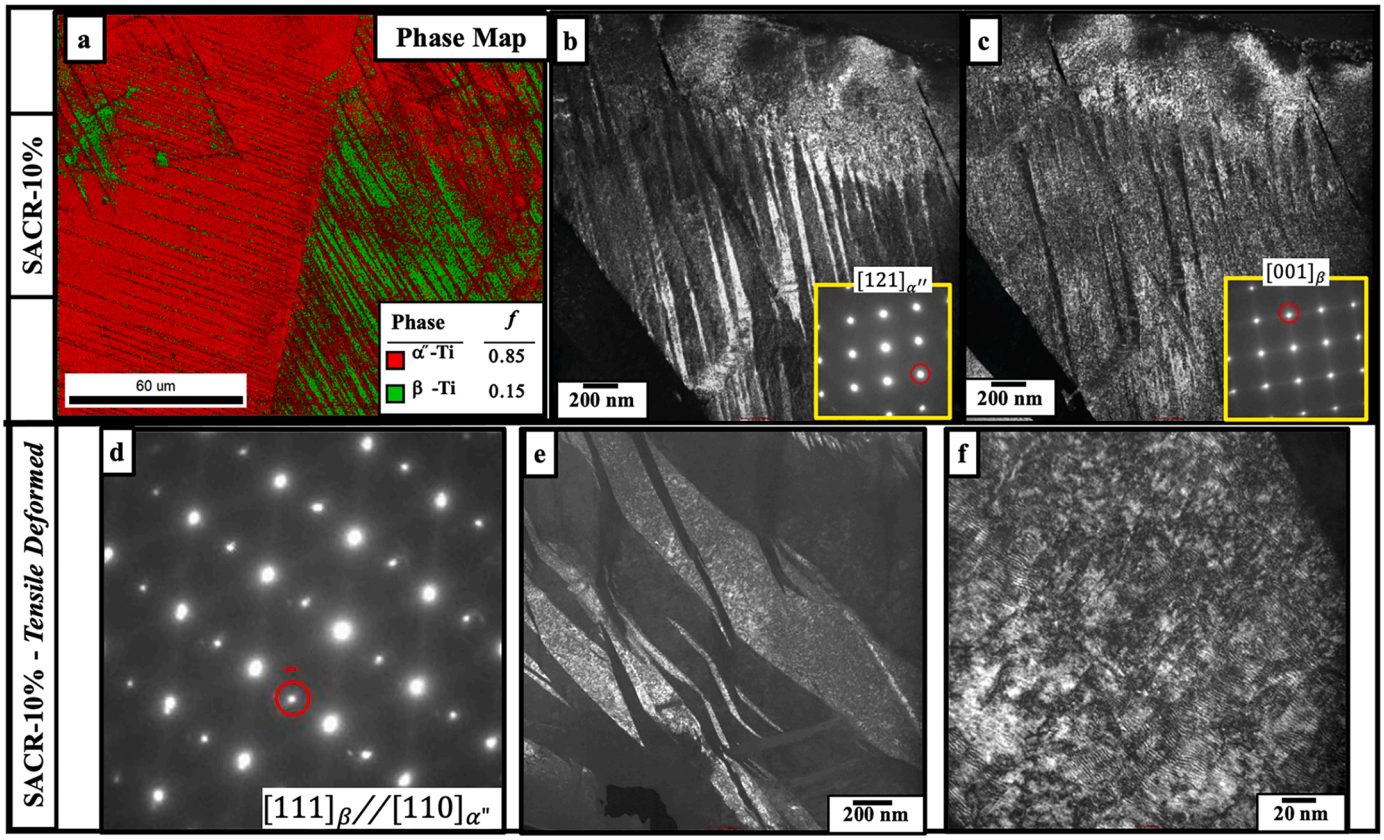

Fig. 5. (a) Phase Map identifying the ***α″*** laths formed in the β−matrix of the SACR-10% condition during the prior cold-rolling, (b) high magnification DFTEM highlighting the ***α″*** laths formed in the same condition, recorded from the spot indicated in the [121]***α″*** ZA SAED pattern shown in the inset and (c) high magnification DFTEM image of the untransformed β-region from the same condition, recorded from the spot indicated in the [001]β ZA SAED pattern shown in the inset. (d) SAED pattern obtained from the overlap of [111]β ZA // [110]***α″***ZA from the SACR-10% condition after tensile deformation. (e) Low and (f) High magnification DFTEM images obtained from the diffraction spot (circled in red) corresponding to ***α″***shown in Fig. 5(d) .

β matrix, thus reducing its metastability with respect to TRIP/TWIP effects and strain-hardenability. In contrast, the cold-rolling leads to the formation of α'' plates within the β matrix, which does not change the matrix composition, consequently maintaining the TRIP/TWIP effects and strain-hardenability in the matrix.

To summarize, a commercial β−titanium alloy, Ti-10V-2Fe-3Al, which exhibits TRIP/TWIP, has been cold-rolled to various percentages (5,10, 20, and 30) with the aim of increasing the YS while preserving its strain hardenability and ductility to varying degrees. The 30% cold-rolled condition exhibits an extraordinarily high YS of ~1800 MPa but virtually no tensile ductility. While the 20% cold-rolled condition exhibited reasonably high YS (~1500 MPa) with limited ductility (3%), the 5% and 10% rolled conditions offered the best combination of YS and ductility. Detailed microstructural characterization has been performed to understand the differences in the stress-induced products formed during cold-rolling versus during uniaxial tensile loading, leading to the high strain hardening rates. The results indicate that cold working can be an effective mechanism to tailor the YS in these alloys, while preserving strain-hardenability and ductility via TRIP/TWIP mechanisms.

Declaration of Competing Interest

The authors declare that they have no known competing financial interests or personal relationships that could have appeared to influence the work reported in this paper.

Acknowledgments

The work was supported by two cooperative agreements between the US Army Research Laboratory (ARL) and the University of North Texas (grant numbers W911NF-19–2–0011 and W911NF-16–2–0189) and another grant from the National Science Foundation (NSF), Division of Materials Research (DMR-1905844). The authors would also like to acknowledge the DOE's Advanced Proton Source at the Argonne National Lab for providing access and user time on the beam line for x-ray diffraction experiments.

Supplementary materials

Supplementary material associated with this article can be found, in the online version, at doi:10.1016/j.scriptamat.2022.114890.

References

[1] O.M. Ivasishin, P.E. Markovsky, Y.V. Matviychuk, S.L. Semiatin, C.H. Ward, S. Fox, J. Alloys Compd. 457 (2008) 296–309.
[2] G. Welsch, R. Boyer, E.W. Collings, Materials Properties Handbook: Titanium Alloys, ASM international, 1993.
[3] B. Ellyson, J. Klemm-Toole, K. Clarke, R. Field, M. Kaufman, A. Clarke, Scr. Mater. 194 (2021), 113641.
[4] S.A. Mantri, D. Choudhuri, T. Alam, G.B. Viswanathan, J.M. Sosa, H.L. Fraser, R. Banerjee, Scr. Mater. 154 (2018) 139–144.
[5] M.S.K.K.Y. Nartu, S. Dasari, A. Sharma, S.A. Mantri, S. Sharma, M.V. Pantawane, B. McWilliams, K. Cho, N.B. Dahotre, R. Banerjee, Mater. Sci. Eng. A 821 (2021), 141627.
[6] S. Ozan, J. Lin, Y. Zhang, Y. Li, C. Wen, J. Mater. Res. Technol. 9 (2020) 2308–2318.
[7] I. Weiss, S.L. Semiatin, Mater. Sci. Eng. A 243 (1998) 46–65.

[8] R. Gaur, R.K. Gupta, V. AnilKumar, S.S. Banwait, J. Mater. Eng. Perform. 27 (2018) 3217–3233.
[9] S. Dai, Y. Wang, F. Chen, X. Yu, Y. Zhang, Mater. Sci. Eng. A 575 (2013) 35–40.
[10] W. Zhang, P. Yang, X. Liang, Y. Cao, S. Ouyang, Y. Liu, Z. Wu, J. Alloys Compd. 835 (2020), 155332.
[11] H. Matsumoto, S. Watanabe, S. Hanada, J. Alloys Compd. 439 (2007) 146–155.
[12] T.W. Duerig, G.T. Terlinde, J.C. Williams, Metall. Trans. A 1980 (2013) 1987–1998, 1112 11.
[13] T.W. Duerig, J. Albrecht, D. Richter, P. Fischer, Acta Metall 30 (1982) 2161–2172.
[14] J.D. Cotton, R.D. Briggs, R.R. Boyer, S. Tamirisakandala, P. Russo, N. Shchetnikov, J.C. Fanning, JOM 676 (67) (2015) 1281–1303, 2015.
[15] S.A. Mantri, M.S.K.K.Y. Nartu, S. Dasari, A. Sharma, P. Agrawal, R. Salloom, F. Sun, E. Ivanov, K. Cho, B. McWilliams, S.G. Srinivasan, N.B. Dahotre, F. Prima, R. Banerjee, Addit. Manuf. 48 (2021), 102406.
[16] L. Qi, X. Qiao, L. Huang, X. Huang, X. Zhao, Mater. Sci. Eng. A 756 (2019) 381–388.
[17] S. Neelakantan, D. San Martin, P.E.J. Rivera-Díaz-del-Castillo, S. van der Zwaag, Mater. Sci. Technol. 25 (2009) 1351–1358.
[18] R.R. Boyer, G.W. Kuhlman, Metall. Trans. A 18 (1987) 2095–2103.
[19] Y. Danard, R. Poulain, M. Garcia, R. Guillou, D. Thiaudière, S. Mantri, R. Banerjee, F. Sun, F. Prima, Materialia 8 (2019), 100507.
[20] F. Sun, J.Y. Zhang, M. Marteleur, C. Brozek, E.F. Rauch, M. Veron, P. Vermaut, P. J. Jacques, F. Prima, Scr. Mater. 94 (2015) 17–20.
[21] M. Marteleur, F. Sun, T. Gloriant, P. Vermaut, P.J. Jacques, F. Prima, Scr. Mater. 66 (2012) 749–752.
[22] T. Akanuma, H. Matsumoto, S. Sato, A. Chiba, I. Inagaki, Y. Shirai, T. Maeda, Scr. Mater. 67 (2012) 21–24.
[23] C. Li, J. Chen, Y.J. Ren, W. Li, J.J. He, J.H. Chen, J. Alloys Compd. 641 (2015) 192–200.